

# Trapping and amplification of unguided mode EMIC waves in the radiation belt

Geng Wang (✉ [wanggeng@hit.edu.cn](mailto:wanggeng@hit.edu.cn))

Institute of Space Science and Applied Technology, Harbin Institute of Technology

Zhonglei Gao

School of Physics and Electronic Sciences, Changsha University of Science and Technology

Mingyu Wu

Harbin Institute of Technology, Shenzhen

Guoqiang Wang

Harbin Institute of Technology, Shenzhen

Sudong Xiao

Institute of Space Science and Applied Technology, Harbin Institute of Technology, Shenzhen

Yuanqiang Chen

Department of Geophysics and Planetary Sciences, University of Science and Technology of China

Zhengyang Zou

Institute of Space Science and Applied Technology, Harbin Institute of Technology

Tielong Zhang

Institute of Space Science and Applied Technology, Harbin Institute of Technology, Shenzhen

---

## Article

**Keywords:** electromagnetic ion cyclotron (EMIC), radiation belt

**Posted Date:** January 21st, 2021

**DOI:** <https://doi.org/10.21203/rs.3.rs-132689/v1>

**License:**  This work is licensed under a Creative Commons Attribution 4.0 International License.

[Read Full License](#)

---

**Version of Record:** A version of this preprint was published at Journal of Geophysical Research: Space Physics on August 27th, 2021. See the published version at <https://doi.org/10.1029/2021JA029322>.

1    **Trapping and amplification of unguided**  
2    **mode EMIC waves in the radiation belt**

3

4

### Abstract

5    Electromagnetic ion cyclotron (EMIC) waves can cause the scattering  
6    loss of the relativistic electrons in the radiation belt. They can be clas-  
7    sified into the guided mode and the unguided mode, according to waves  
8    propagation behavior. The guided mode waves have been widely inves-  
9    tigated in the radiation belt, but the observation of the unguided mode  
10   waves have not been expected. Based on the observations of Van Allen  
11   Probes, we demonstrate for the first time the existence of the intense un-  
12   guided mode EMIC waves in the radiation belt. Growth rate analyses  
13   indicate that the hot protons with energies of a few hundred keV may  
14   provide the free energy for wave growth. The reflection interface formed  
15   by the spatial locations of local helium cutoff frequencies can be nearly  
16   parallel to the equatorial plane when the proton abundance ratio decreas-  
17   es sharply with  $L$ -shell. This structure combined with hot protons may  
18   lead to the trapping and significant amplification of the unguided mode  
19   waves. These results may help to understand the nature of EMIC waves  
20   and their dynamics in the radiation belt.

21 **Introduction**

22 The earth radiation belt is dynamically influenced by multiple types of waves,  
23 one of them is the electromagnetic ion cyclotron (EMIC) wave, which has been  
24 widely investigated in recent decades [1–9], and has been considered to have  
25 the potential to remove the relativistic electrons from the radiation belt over a  
26 time-scale of several hours [10–20].

27 The typical EMIC waves have often been observed just below the hydrogen  
28 ( $H^+$ ) gyrofrequencies ( $f_{cH+}$ ), with left-hand polarizations (L-mode) and quasi-  
29 parallel wave vectors [3, 5, 7]. In the radiation belt, the existence of minor ions  
30 ( $He^+$  and  $O^+$ ) separate the cold plasma dispersion curves of EMIC waves into  
31 several branches, and the L-mode EMIC waves can belong to two types of  
32 propagation modes: one is the guided mode and the other is the unguided mode  
33 (Supplementary Fig.1), according to whether the wave group velocity is guided  
34 by the ambient magnetic field [21, 22]. The guided mode waves can propagate  
35 in the same  $L$ -shell within which the substorm injected hot ions are trapped.  
36 The anisotropic hot  $H^+$  with the energy of tens of keV can resonate with the  
37 waves of guided mode, and lead to the wave growth [21, 23–30]. Moreover, the  
38 anisotropic  $H^+$  distributions induced by the magnetospheric compression may  
39 also lead to the generation of guided mode EMIC waves close to  $f_{cH+}$  [2, 31–35].  
40 Therefore, the commonly observed EMIC waves are widely investigated based  
41 on the guided mode [36–40].

42 Simulations have suggested that the convective amplification of the unguided  
43 mode waves will not be significant, as the wave normal angle increases very  
44 quickly and the waves rapidly move to larger  $L$ -shell [21, 22, 40]. Moreover, as  
45 the wavenumber of the unguided mode is relatively larger than that of the guided  
46 mode (Supplementary Fig.1), the resonant energy may exceed the peak energy  
47 of the substorm injected hot  $H^+$ , which does not favor the wave generation.

48 Up to now, the investigations of unguided mode EMIC waves in the radia-  
49 tion belt have been ignored. However, the hot  $H^+$  with hundreds of keV can  
50 inject into the ring current during storms [41], theoretically providing the energy  
51 source for the generation of unguided mode waves. Moreover, the smaller group  
52 velocities of unguided mode waves may lead to the larger convective growth  
53 rates, which can favor the wave generation [42].

54 The motivation of the present study is based on the following questions:  
55 Can we find the distinguishable unguided mode EMIC waves that are locally  
56 generated below  $f_{cH+}$ ? If so, what's the difference of the generation mechanism  
57 between the guided and unguided mode waves? Here we identify the existence of  
58 the intense unguided mode EMIC waves in the earth's radiation belt by present-  
59 ing Van Allen Probe [43] observations. We will propose that the generation of  
60 these waves are associated with a new type of wave trapping mechanism, which  
61 is controlled by the spatial variation of ion abundance ratios. In the discussion  
62 section, we will focus on the question that whether the unguided mode EMIC  
63 waves are common in the radiation belt.

64 **Results**

65 **Overview of the Event**

66 As shown in Figure 1a, the event was observed by Probe A on 15 December  
67 during the recovery phase of a magnetic storm, after at least three suc-  
68 cessive prominent substorms where  $AE > 500$  nT. In Figure 1b–c, the hot  $H^+$   
69 fluxes detected by the Radiation Belt Storm Probes Ion Composition Experi-  
70 ment (RBSPICE) instrument [44] and the Helium, Oxygen, Proton, and Electron  
71 (HOPE) mass spectrometer [45], enhance in four distinct energy ranges: below  
72 10 keV, 10 – 30 keV, 30 – 100 keV and 100 – 600 keV. The peak energy of  
73 the hot  $H^+$  for each energy range decreases with  $L$ -shell, indicating the energy-  
74 dispersive substorm injected ions [41]. From Figure 1d, the satellite passed  
75 through the plasmapause at  $L \sim 2.87$ , and the background electron number  
76 density  $n_e$  which was measured by the High Frequency Receiver (HFR) [46] of  
77 the Electric and Magnetic Field Instrument and Integrated Science (EMFISIS)  
78 suite [47], dropped from  $\sim 100$  cm $^{-3}$  at just outside the plasmapause to  $\sim 20$   
79 cm $^{-3}$  at  $L \sim 3.7$ . Measured by the triaxial fluxgate magnetometer (MAG) of  
80 EMFISIS, the conspicuous  $H^+$  band waves appear from  $L \sim 3.1$  to  $L \sim 3.7$ , as  
81 exhibited in Figure 1e. These waves with quasi-constant frequencies appear to  
82 be intense just outside the plasmapause and decay gradually with the increasing  
83  $L$ -shell.

84 **Wave analyses and Ion Abundance Ratios**

85 The detailed wave properties are exhibited in Figure 2. In general, the time  
86 series of the wave spectra can be divided into three distinct regions based on the  
87 observational characteristics, as marked by the blue boxes. The Region A waves  
88 appear at MLAT  $\sim -1.5$ , have the strongest magnetic spectral density  $PSD_B$ ,  
89 associated with the quasi-parallel wave normal angle  $\psi$  and small compressional  
90 ratio  $PSD_{B\parallel}/PSD_B$ , indicating that they were propagating roughly along the  
91 axis perpendicular to the equatorial plane. Furthermore, the general direction  
92 (shown by the diamonds, which are the spectrum-weighted averages) of the  
93 Poynting fluxes appears to be northward for the inner waves, and be southward  
94 for the outer waves, as shown in Figure 2f. The Poynting fluxes for almost all  
95 these intense waves possess an inward orientation according to Figure 2e. The  
96 results of the ellipticity  $\epsilon_B$  show predominately left-hand polarization, indicating  
97 that the waves belong to the L-mode. As the satellite moved away from the  
98 Earth, Region B waves were observed in successive time series, but these waves  
99 show a decrease in  $PSD_B$  of approximately one order. The most outstanding  
100 phenomena are recorded in the  $\epsilon_B$  spectra, where the waves exhibit left-hand  
101 polarization inside  $L = 3.46$  but right-hand polarization outside. There is a  
102 sharp boundary that roughly shifts from a higher frequency at inner  $L$  to a  
103 lower frequency at outer  $L$ . This phenomenon may indicate the pass-through of  
104 the  $He^+$  crossover frequency  $f_{crHe+}$ , and the waves with right-hand polarization  
105 should belong to the R-mode. Independent of the polarization, the waves with

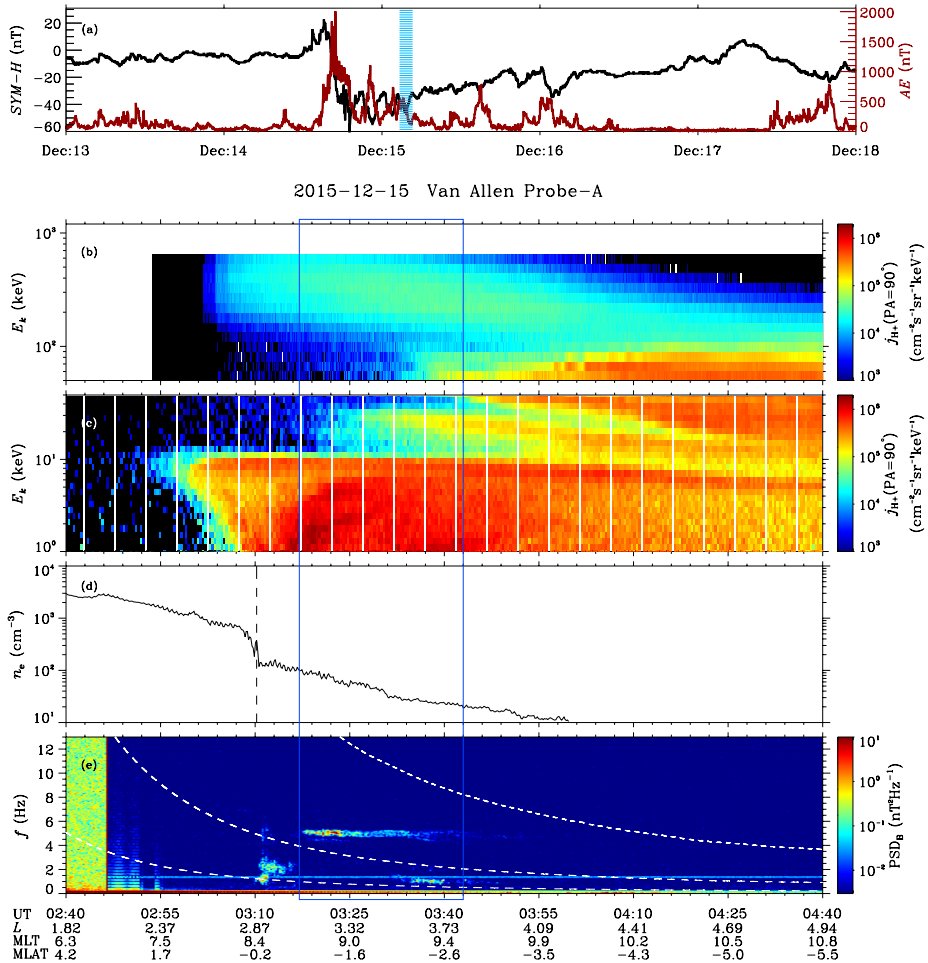


Figure 1: Overview of the background conditions of the wave event recorded by Van Allen Probe A on 15 December 2015 : (a) SYM-H index and AE index (shaded region marks the period of the wave event). (b) Background electron number density  $n_e$  (dashed lines for the location of the plasmapause). (c,d) Energy-dependent  $H^+$  differential fluxes  $j_{H^+}$  at a  $90^\circ$  pitch angle measured by RBSPICE and ECT HOPE. (e) Magnetic power spectral density  $PSD_B$ . The white dashed curves trace the local gyrofrequencies of hydrogen, helium, and oxygen. The blue box marks the period of the wave event.

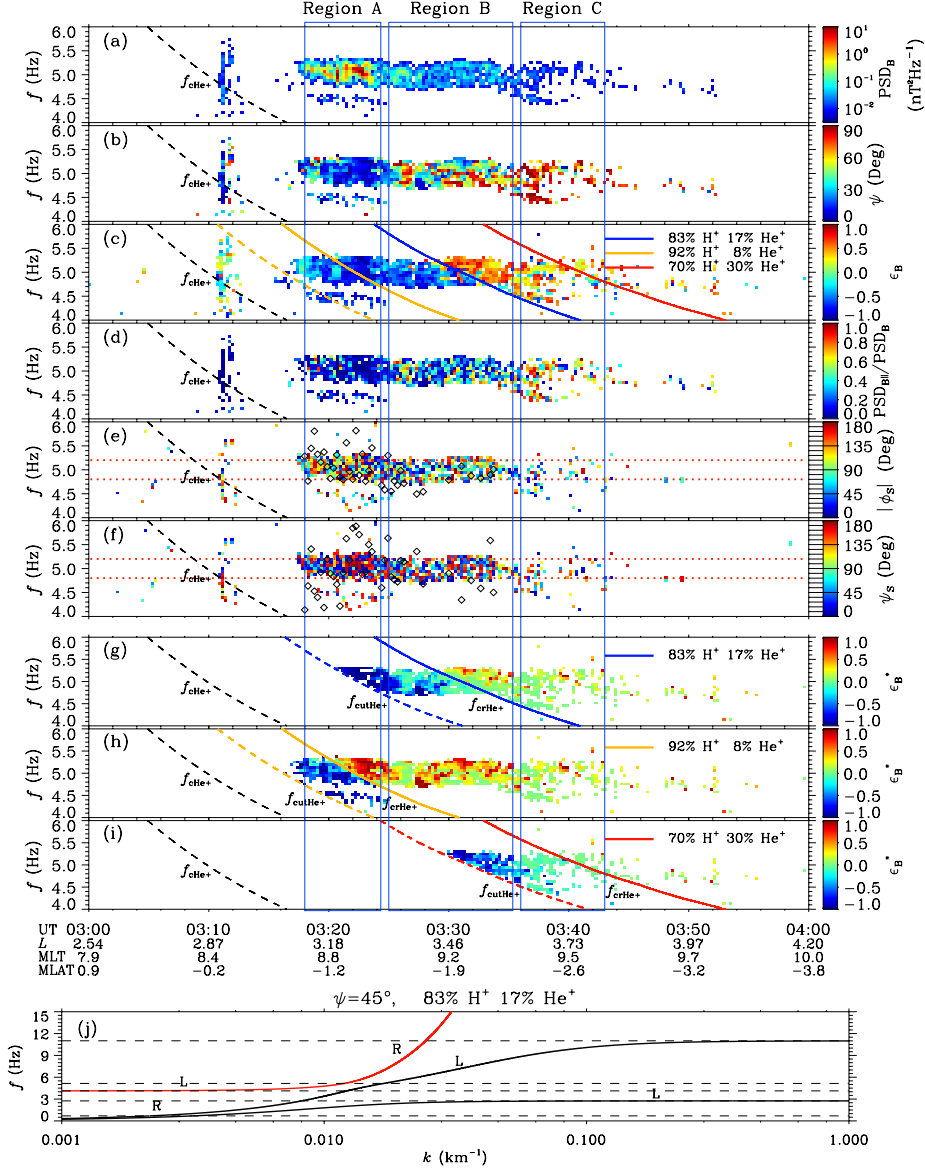


Figure 2: Analyses of wave properties and wave mode. (a) Magnetic power spectral density  $\text{PSD}_B$ . The blue boxes roughly separate the three distinct regions with different observational characteristics. (b) Wave normal angle  $\psi$  (unifying the two field-aligned orientations). (c) Wave ellipticity  $\epsilon_B$ . (d) Wave magnetic compression ratio  $\text{PSD}_{B\parallel}/\text{PSD}_B$ . (e) The azimuthal angle of the Poynting flux  $\phi_S$  ( $0^\circ$  represents away from the Earth). (f) The angle of the Poynting flux with respect to the ambient magnetic field  $\psi_S$ . Black diamonds in (e) and (f) are the spectrum-weighted averaged angles within the frequency range of  $4.8 - 5.2$  Hz (red dotted lines), and they share the same axis with the corresponding color bars. (g-i) The theoretically calculated distribution of the ellipticity  $\epsilon_B^*$  for the given ion abundance ratios. The colored solid and dashed lines trace the local crossover frequencies  $f_{\text{crHe+}}$  and cutoff frequencies  $f_{\text{cutHe+}}$ . (j) Dispersion relations under the observed plasma conditions. The red curve represents the observed wave mode. The letter ‘L’ and ‘R’ denote the left-hand and right-hand polarizations, respectively.

106 different values of the wave normal angle  $\psi$  or compressional ratio  $\text{PSD}_{B\parallel}/$   
107  $\text{PSD}_B$  are highly mixed. Moreover, the spectrum-weighted averaged angles  
108 of Poynting fluxes point mainly away from the Earth or along the azimuthal  
109 direction (Figure 2e), with a relatively small angle with respect to the equatorial  
110 plane (Figure 2f). The outermost waves are presented in Region C, with a wave  
111 power 2 orders of magnitude smaller than that of the waves in Region A. The  
112 wave vectors are almost perpendicular to the ambient field, the compressional  
113 ratios are relatively large, and the polarizations are predominantly right-handed,  
114 indicating these are the oblique R-mode waves.

115 With increasing  $L$ -shell value, the relative frequency  $f/f_{cH^+}$  increases for the  
116 observed  $H^+$  band waves with a quasi-constant frequency, and the polarization  
117 mode thus changes from L-mode to R-mode. Such a phenomenon indicates that  
118 the waves belong to the unguided mode [21], as illustrated in Figure 2j. Here, we  
119 perform the plasma diagnostics to verify the wave mode and estimate the ion  
120 abundance ratios  $\eta_s$ . As shown by Figure 2c, a series of  $f_{\text{crHe}+}$  (and also cutoff  
121 frequencies  $f_{\text{cutHe}+}$ ) can be obtained for a given group of  $\eta_s$ . Assuming that  
122 the boundary where the polarization reversal takes place (the blue solid curve)  
123 represents the trace of  $f_{\text{crHe}+}$ , one can obtain  $\eta_{H^+} \sim 83\%$  and  $\eta_{He^+} \sim 17\%$ .  
124 Substituting the obtained  $\eta_s$  and the observed  $\psi$  (Figure 2b) into Equations  
125 (2) and (7), one can obtain the theoretically estimated ellipticity  $\epsilon_B^*$ . As shown  
126 in Figure 2g, the polarization reversal boundary does exist for the  $\epsilon_B^*$  spectra  
127 and generally matches the observed boundary. However, the waves observed  
128 before 03:20 UT can not be seen in the predicted spectra, suggesting that the  
129 cutoff frequencies are overestimated. Considering that the background plasma  
130 density decreases prominently with  $L$  in the range where the wave exists (Figure  
131 1d), one can assume that  $\eta_s$  may also vary with  $L$ . Assuming that the cutoff  
132 frequencies lie just below the lowest frequencies of the observed intense waves,  
133 a group of  $\eta_s$  can be obtained by Equation (8): 92%  $H^+$  and 8%  $He^+$ . As  
134 shown in Figure 2h, the predicted spectra contain the lower-frequency waves  
135 observed before 03:20 UT, but the predicted polarization reversal boundary  
136 does not match the observed boundary. In addition, a group of  $\eta_s$  is provided in  
137 Figure 2i for comparison, where both the cutoff frequency and the polarization  
138 distribution deviate from the observations significantly. These results suggest  
139 that the  $H^+$  abundance decreases from at least 92% at  $L \sim 3.2$  to approximately  
140 83% at  $L \sim 3.5$  where the polarization reversal takes place. Furthermore, these  
141 results verify that the observed waves should belong to the unguided mode, and  
142 the polarization reversal boundary is indeed the time series of  $f_{\text{crHe}+}$ .

143 Two possible scenarios can explain the above phenomena. First, the source  
144 is in Region A, and the waves in Region B and Region C are the leaked waves  
145 from the source, as they are not guided by the ambient magnetic field. Second,  
146 the waves in Region A are parallelly excited while the waves in Region B and  
147 Region C are obliquely excited.

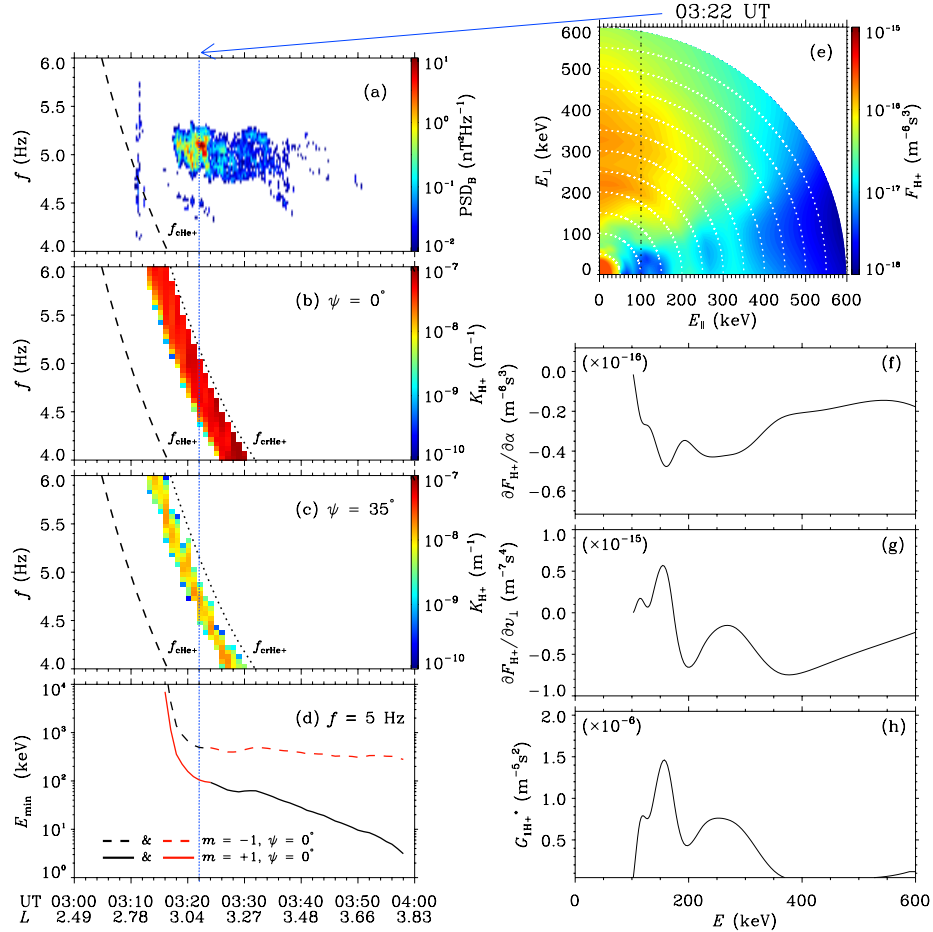


Figure 3: Wave growth analyses. (a) The observed magnetic power spectral density  $PSD_B$ . (b-c) Wave convective growth rates  $K_{H+}$  contributed by  $H^+$  at different wave normal angles. The dotted curves trace the  $He^+$  crossover frequencies while the dashed curves trace the  $He^+$  gyrofrequencies. (d) Minimum  $H^+$  resonant energy  $E_{\min}$  at a wave frequency of  $f = 5$  Hz for different resonant orders. The red curves mark the resonance for the current unguided mode. (e) Distribution of the observed  $H^+$  phase space density  $F_{H+}$  in the  $E_\perp - E_\parallel$  space at the time point 03:22 UT. The dotted line represents the resonant surface for the fundamental resonance at the wave normal angle  $\psi = 0^\circ$ . (f-h) Energy dependence of  $\partial F_{H+}/\partial \alpha$ ,  $\partial F_{H+}/\partial v_\perp$  and  $G_{1H+}^*$  along the resonant surface as shown in (e). Here  $\alpha$  is the pitch angle,  $v_\perp$  is the perpendicular velocity of  $H^+$ , and  $G_{1H+}^*$  is the integrating factor in the growth rate expression.

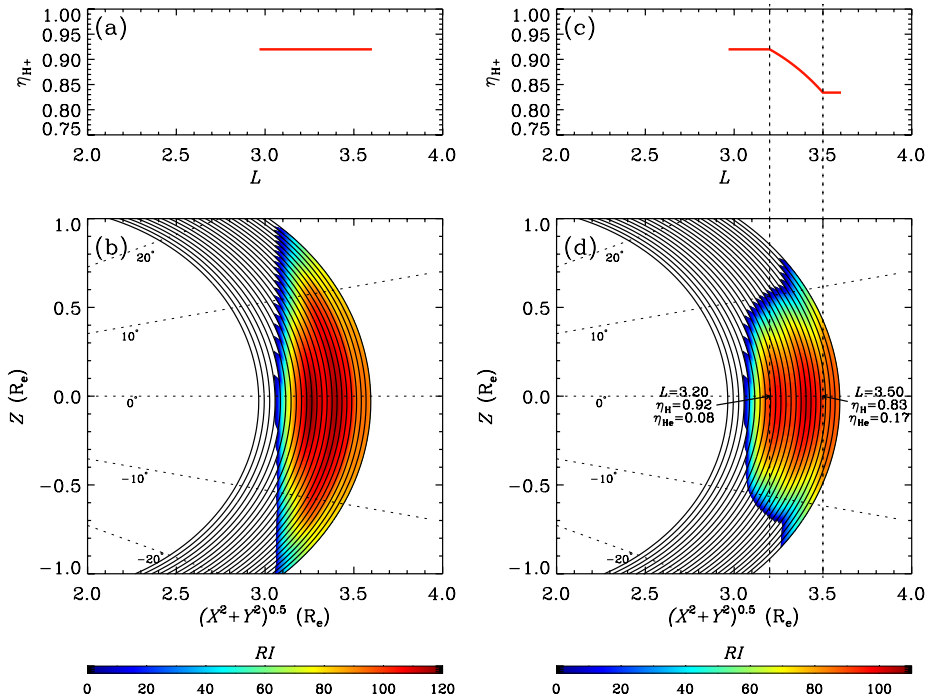


Figure 4: The distribution of the refractive index  $RI$  in a plasma environment with the ion abundance ratio  $\eta_{\text{H}^+}$ : (a,b) distributed uniformly and (c,d) varied with the  $L$ -shell. The coordinate system is established in the Earth's dipole field: the horizontal axis represents the radial distance to the dipole axis, while the  $Z$  axis is along the dipole axis. Solid black curves trace the background magnetic field estimated with the help of the T89 model.

## 148 Wave Growth Mechanism

149 To reveal the generation mechanism of the observed unguided mode waves,  
150 we first present the results of the linear convective growth rate in Figure 3.  
151 Figure 3b and Figure 3c show the convective growth rate distributions under  
152 the fixed  $\eta_s$ :  $\eta_{H^+} = 92\%$  and  $\eta_{He^+} = 8\%$ . Positive growth rates appear below  
153 the local  $f_{crHe^+}$ , covering the ranges of the observed intense L-mode waves in  
154 the inner  $L$ -shell (Figure 3a). No wave growth can be obtained above  $f_{crHe^+}$ ,  
155 due to the much higher resonant energy between  $H^+$  and R-mode (Figure 3d).  
156 This result eliminates the possibility that the observed oblique R-mode waves  
157 in the outer  $L$ -shell are excited locally. However, the highest magnitude of the  
158 convective growth rate  $K_{H^+}$  is  $\sim 10^{-7} \text{ m}^{-1}$  for the parallel waves, therefore, the  
159 path-integrated wave gain should be a factor of at least  $\sim 10^3$  (7 e-foldings), to  
160 satisfy the growth of the observed intense waves from the background noise level  
161 (according to Figure 3a). This corresponds to an integrated traveling distance  
162 in the source adding up to  $\sim 11 R_E$ .

163 Before the further explanation of wave growth, it is instructive to examine  
164 the exact potential source of the waves. Figure 3e displays the distribution of  
165 phase space density of proton  $F_{H^+}$  and the resonant surface at 03:22 UT. As  
166 the minimum resonant energy is approximately 100 keV for the fundamental  
167 resonance of the parallel left-hand waves, the resonant surface avoids the hot  
168  $H^+$  rings with lower energies, but crosses the ring with the energy range of  $\sim$   
169 200 – 450 keV. The parameters crucial for the growth rate are presented in  
170 Figure 3f-h. The minimum of  $\partial F_{H^+}/\partial\alpha$  and the maximum of  $\partial F_{H^+}/\partial v_\perp$  are  
171 both obtained at  $E_k \sim 180$  keV, where the ring emerges (Figure 3e). The final  
172 value of  $G_{1H^+}^*$  is positive from 100 keV to 350 keV and peaks at  $E_k \sim 180$  keV,  
173 indicating that these hot  $H^+$  with several hundreds of keV contribute to the  
174 potential excitation of the most intense waves in Region A.

175 The waves within the inner  $L$ -shell are intense and predominated by field-  
176 aligned wave vectors and Poynting fluxes but become weaker and more oblique  
177 outside. Moreover, the waves observed in all these regions have almost a con-  
178 stant frequency range. This evidence strongly implies that the waves are gen-  
179 erated inside and propagated outward. The growth rate results further suggest  
180 this assumption by eliminating the possibility of oblique excitation for the outer  
181 right-hand waves. However, the most challenging problem is that the convec-  
182 tive growth rate is too small for the observed strong waves generated in any  
183 potential source region with a limited spatial range. According to the previ-  
184 ous analysis, an integrated traveling distance of  $\sim 11 R_E$  in the source region is  
185 needed for the full growth of the waves. It is reasonable to associate the con-  
186 vective growth process with some kind of wave trapping mechanism. As the hot  
187 ions are trapped in the narrow range of the  $L$ -shell, the azimuthal propagation  
188 of the waves may provide the required integrated distance in one-half of the  
189 drift circle. However, this scenario contradicts the observed parallel component  
190 of the Poynting fluxes. Considering that the intense quasi-parallel waves are  
191 just above the local cutoff frequency  $f_{cutHe^+}$ , where the unguided mode waves  
192 should be reflected. To investigate the possibility of wave trapping, the dis-

tributions of refractive indexes RI are calculated in the simplified background plasma environment. The magnetic fields are estimated using the T89 model, and the values along each filed line are calibrated by multiplying the factor  $B_{\text{obs}}/B_{\text{model}}$  (ratio of the observed and model estimated value at the intersection point between satellite orbit and field line). The density distribution is calculated by  $\rho(MLAT) = \rho_{eq}/\cos(MLAT)$  with the help of the observations. As demonstrated in Figure 4a–b, in a plasma environment with constant  $\eta_s$ , the reflection interface where the refractive indexes RI decrease to zero is approximately perpendicular to the equatorial plane, because the value of  $f_{\text{cutHe+}}/f_{\text{cH+}}$  remains the same while the value of  $f_{\text{cutHe+}}$  decreases with radial distance but increases with latitude due to the variation of the magnetic field. In the present case, the relative frequency  $f_{\text{cutHe+}}/f_{\text{cH+}}$  should increase with  $\eta_{\text{He+}}$  (or decrease of  $\eta_{\text{H+}}$ , as shown in Figure 4c) at a higher  $L$ -shell, thus offsetting the effect of the magnetic field. The strong reflection interface formed by the locations of  $f_{\text{cutHe+}}$  (where RI = 0) is therefore approximately parallel to the equatorial plane, as shown in Figure 4d. The conjugate reflection interfaces in both sides of the equatorial plane may produce a trapping zone, within which some of the unguided mode waves will be trapped and experience the significant amplification to the observed intensity. In addition, as shown in Figure 2b, the plasma number density experiences a sharp change at approximately  $L = 3.48$ , which may result in a dramatic variation in  $\eta_s$  with  $L$ , and thus form a quasi-parallel or even negatively inclined reflection interface at the radial distance  $\sim 3.2 - 3.3 R_E$ . This is consistent with the strongest waves observed at  $L \sim 3.2 - 3.3$  near the equator. Moreover, both the L-mode waves and the R-mode waves in Region B possess almost the same magnitude of wave power (Figure 2), suggesting that they are the leaked waves from the inner trapping region. Following such a scenario, one can predict that the waves observed away from the trapping region should propagate in the direction pointing from the trapping region to the observed position, which can explain the quasi-perpendicular waves observed in Region C.

## Discussion

During the period from September 2013 to May 2018, another obvious event of unguided mode waves with a distinguishable crossover frequency was recorded by Probe A on 30 November 2015, when the satellite was outside the plasmasphere (please see Supplementary Fig.4). A similar trend of the spatial variation of ion abundance ratios can be obtained based on plasma diagnostics (Supplementary Fig.5), indicating the potential existence of wave trapping. The intense L-mode waves are observed along with the enhancement of hot H<sup>+</sup> with the energies of hundreds of keV, while the positive convective growth rates are obtained (Supplementary Fig.6). The magnitude of largest growth rates is approximately several times of  $10^{-7} \text{ m}^{-1}$ , which is inadequate for the waves to be amplified to the observed magnitude (more than 7 e-foldings) in an integrated distance less than 1  $R_E$ . As the waves are observed near the equatorial plane,

236 one can thus predict that the wave trapping mechanism may have played an  
237 important role in the amplification of the observed waves.

238 The event in the previous section was recorded by Probe A. In fact, Probe B  
239 also recorded a wave event in the same area  $\sim 2$  hours ago. As shown in Supple-  
240 mentary Fig.4, the intense  $H^+$  band waves were observed at  $L \sim 3.16$ ,  $MLT \sim$   
241  $8.5$  and  $MLAT \sim -1.2$ , which were within exactly the same area of Probe-A-  
242 event. Comparing Figure 1 and Supplementary Fig.7, the background plasma  
243 conditions are also similar for these two probes during their respective passes,  
244 i.e., waves were observed just outside the plasmasphere, with the enhancement  
245 of hot protons of hundreds of keV. In the event of Probe B, a weak ‘tail’ toward  
246 the higher  $L$ -shell and larger value of  $f/f_{cH^+}$  can also be observed. This ‘tail’  
247 can be explained by the outward propagation of the unguided mode waves. In  
248 addition, the intense waves are separated by an area where the signals are weak  
249 (Supplementary Fig.7e). In the meanwhile, the spatial fluctuation of density is  
250 obvious (Supplementary Fig.7b), which may indicate the sharp variation of ion  
251 abundance ratios. In this event, however, no obvious boundary of R-mode and  
252 L-mode can be distinguished, as shown in Supplementary Fig.8. Therefore, we  
253 can not determine the mode of these waves based on the observations. However,  
254 as the plasma conditions are the same as that of Probe-A-event, and the weak  
255 ‘tail’ may indicate the propagation toward higher  $L$ -shell, it is reasonable to  
256 suppose that these waves are the unguided mode waves, being trapped and am-  
257 plified with the same mechanism as the waves in Probe-A-event (Supplementary  
258 Fig.9 and Supplementary Fig.10 show the growth rates). If so, as these waves  
259 do not have an obvious right-hand polarization, they can not be distinguished  
260 from the guided mode waves, maybe they are common in the radiation belt and  
261 are intermixed with the guided mode waves in the previous studies. The exact  
262 measurements of ion abundance ratios are needed for further identification of  
263 these different modes.

264 From previous studies, the guided mode EMIC waves can scatter relativistic  
265 electrons via cyclotron resonance [48–52] or bounce resonance [53], and are finally  
266 damped by heating the  $\sim 10$  keV ring current ions via harmonic cyclotron reso-  
267 nances [54] or by heating the cold electrons up to a few hundred eV via Landau  
268 resonance [10, 55]. In the present event, the wavenumber of the intense L-mode  
269 waves is approximately  $1 \times 10^{-5} \text{ m}^{-1}$  (Figure 4f), and the non-relativistic elec-  
270 tron gyrofrequency is approximately 24 kHz, therefore, the minimum resonant  
271 energy for the relativistic electrons is  $\sim 10$  MeV, corresponding to the highest  
272 energy of the relativistic electrons that have been detected [56]. In addition,  
273 as some waves could leak away from the source and propagate to the higher  
274  $L$ -shell in an intermediate wave normal angle, if the background density does  
275 not decrease significantly, the parallel wavenumber should remain relatively un-  
276 changed while the electron gyrofrequency experiences a rapid decrease. In this  
277 case, one can predict a resonant scattering of the MeV electrons by the waves,  
278 in the core region of the radiation belt ( $L \sim 4.0 - 5.0$ ). In summary, the present  
279 study clearly demonstrates the existence of unguided mode EMIC waves in the  
280 radiation belt, and propose a trapping and amplification mechanism for explain-  
281 ing their origin. The results may have potential importance in the dynamics of

<sup>282</sup> the earth's radiation belt, and may provide inspiration for the investigations of  
<sup>283</sup> the EMIC waves in the magnetosphere of other planets.

## <sup>284</sup> Methods

### <sup>285</sup> Extraction of Wave Properties

<sup>286</sup> The magnetic field data from MAG, and the electric field data from EFW are  
<sup>287</sup> used to analyze the wave properties. The 64 Hz magnetic field data are processed  
<sup>288</sup> through a 1024-point fast Fourier transform (FFT, without detrending) to ob-  
<sup>289</sup> tain the magnetic spectral matrix. Singular value decomposition (SVD) analysis  
<sup>290</sup> [57] is performed on the magnetic spectral matrix to estimate the wave normal  
<sup>291</sup> angle, azimuthal angle, and wave polarization [57]. The 32 Hz two-dimensional  
<sup>292</sup> electric field data from EFW are used to estimate the vector electric field, and  
<sup>293</sup> the spin axis-aligned component is estimated with the assumption that  $\mathbf{E} \cdot \mathbf{B} = 0$ .  
<sup>294</sup> Then, a 512-point FFT is carried out for both the electric field and the mag-  
<sup>295</sup> netic field (resampled to 32 Hz) to obtain the cross-power spectra, and thus, we  
<sup>296</sup> obtain the Poynting vector [58].

### <sup>297</sup> Plasma Diagnostics

<sup>298</sup> In the cold plasma, the following Stix parameters are helpful to investigate the  
<sup>299</sup> dispersion relation [59]:

$$L = 1 - \sum_s \frac{\omega_{ps}^2}{\omega(\omega - \Omega_s)}, \quad R = 1 - \sum_s \frac{\omega_{ps}^2}{\omega(\omega + \Omega_s)}, \quad P = 1 - \sum_s \left( \frac{\omega_{ps}}{\omega} \right)^2, \quad (1)$$

<sup>300</sup> here  $\omega_{ps} = (n_s q_s^2 / m_s \epsilon_0)^{\frac{1}{2}}$  and  $\Omega_s = q_s B / m_s$  are respectively the plasma  
<sup>301</sup> frequency and the gyrofrequency of a particle species s.

<sup>302</sup> The crossover frequency  $f_{cr}$  and the cutoff frequency  $f_{cut}$  can connect the  
<sup>303</sup> observations to the dispersion relation.  $f_{cr}$  is the frequency where the L-mode  
<sup>304</sup> and R-mode phase velocities are equal [60] and can be obtained by setting the  
<sup>305</sup> Stix parameter L equal to R:

$$\sum_s \frac{\omega_{ps}^2}{\omega_{cr}(\omega_{cr} - \Omega_s)} = \sum_s \frac{\omega_{ps}^2}{\omega_{cr}(\omega_{cr} + \Omega_s)}. \quad (2)$$

<sup>306</sup> Considering the charge neutrality condition, the determination of full ion  
<sup>307</sup> abundance ratios requires the values of at least two characteristic frequencies  
<sup>308</sup> (except gyrofrequencies) to be known in H<sup>+</sup>, He<sup>+</sup> and O<sup>+</sup> plasma. However, if  
<sup>309</sup> the O<sup>+</sup> abundance  $\eta_{O+}$  is much lower than the H<sup>+</sup> abundance  $\eta_{H+}$  and if the  
<sup>310</sup> focused mode belongs to the H<sup>+</sup> band which has a much larger frequency than  
<sup>311</sup> the oxygen gyrofrequency  $\Omega_{O+}$ , then we have the following relations:

$$-\frac{\omega_{pH+}^2}{\omega(\omega - \Omega_{H+})} \gg \frac{\omega_{pO+}^2}{\omega(\omega - \Omega_{O+})}, \quad \text{when } \Omega_{He+} < \omega < \Omega_{H+} \quad (3)$$

312

$$\frac{\omega_{\text{pHe+}}^2}{\omega(\omega - \Omega_{\text{He+}})} \gg \frac{\omega_{\text{pO+}}^2}{\omega(\omega - \Omega_{\text{O+}})}, \text{ when } \omega \rightarrow \Omega_{\text{He+}} \quad (4)$$

313

$$\frac{\omega_{\text{pH+}}^2}{\omega(\omega + \Omega_{\text{H+}})} \gg \frac{\omega_{\text{pO+}}^2}{\omega(\omega + \Omega_{\text{O+}})}, \text{ when } \Omega_{\text{He+}} < \omega < \Omega_{\text{H+}} \quad (5)$$

314

$$\frac{\omega_{\text{pH+}}^2}{\omega^2} \gg \frac{\omega_{\text{pO+}}^2}{\omega^2}, \text{ when } \Omega_{\text{He+}} < \omega < \Omega_{\text{H+}}. \quad (6)$$

315 Therefore, if the three-ion ( $\text{H}^+$ ,  $\text{He}^+$  and  $\text{O}^+$ ) plasma are approximated as two-  
 316 ion ( $\text{H}^+$  and  $\text{He}^+$ ) plasma, i.e., the terms with oxygen plasma frequency  $\omega_{\text{pO+}}$   
 317 are dropped in Equation (1), the Stix parameters will have only a negligible  
 318 change (example in Supplementary Fig.2). Under such an approximation, a  
 319 group of ion abundance ratios ( $\eta_{\text{H+}}$  and  $\eta_{\text{He+}}$ ) can be obtained by substituting  
 320 the observed value of  $\omega_{\text{crHe+}}/\Omega_{\text{H+}}$  into Equation (2). Consequently, the  
 321 approximated dispersion relations for the modes in  $\text{H}^+$  band can be found.

322 As the wave magnetic field vector is always perpendicular to the wave vector  
 323 (i.e.,  $\mathbf{B} \cdot \mathbf{k} = 0$ ), it is reasonable to define the polarization in terms of the wave  
 324 magnetic field, which is perpendicular to  $\mathbf{k}$ . As the sense of wave field rotation  
 325 about the ambient magnetic field  $\mathbf{B}_0$  remains the same for a certain polarization  
 326 mode, it is convenient to define the handedness in terms of  $\mathbf{B}_0$ . Based on  
 327 these considerations, the polarization state can be represented by the ellipticity  
 328  $\epsilon_B$ , where negative values represent left-hand polarization (see Supplementary  
 329 Figure 1).  $\epsilon_B$  changes sign upon crossing  $f_{\text{cr}}$ . For the observed polarization  
 330 reversal, a validation of whether it represents the crossover frequency  $f_{\text{cr}}$  can be  
 331 performed by comparing the distribution of the observed ellipticity  $\epsilon_B$  with the  
 332 theoretically predicted ellipticity  $\epsilon_B^*$ . In the coordinate system with the z-axis  
 333 along  $\mathbf{B}_0$  and the y-axis perpendicular to the  $\mathbf{B}_0 - \mathbf{k}$  plane, the ratio of the  
 334 wave magnetic field can be expressed as [61, 62]:

$$\frac{B_x}{B_y} = -\frac{(R-L)(P-n^2 \sin^2 \psi)}{P(R+L-2n^2)}, \quad (7)$$

335 where  $\psi$  is the wave normal angle. The field amplitude can be transformed into  
 336 the coordinate system with the z-axis along  $\mathbf{k}$ :

$$B'_x = \frac{B_x}{\cos \psi}, \quad B'_y = B_y, \quad (8)$$

337 the theoretically predicted ellipticity  $\epsilon_B^*$  is then obtained considering that  $B'_x$   
 338 and  $B'_y$  are axes of the polarization ellipse.

339 In summary, the ion abundance ratios are estimated as follows: first, estimate  
 340 the potential crossover frequency from the observed polarization of  $\text{H}^+$   
 341 band waves; then, estimate the  $\text{H}^+$  and  $\text{He}^+$  abundance ratios by Equation

<sup>342</sup> (1); finally, compare the observed ellipticity  $\epsilon_B$  with the calculated theoretical  
<sup>343</sup> ellipticity  $\epsilon_B^*$  for verification.

<sup>344</sup> The cutoff frequency  $f_{\text{cut}}$  is the frequency where the phase velocity equals to  
<sup>345</sup> zero [smith1964propagation], and can be obtained by setting the Stix parameter  
<sup>346</sup>  $L$  equal to zero:

$$1 - \sum_s \frac{\omega_{\text{ps}}^2}{\omega_{\text{cut}}(\omega_{\text{cut}} - \Omega_s)} = 0. \quad (9)$$

<sup>347</sup> Theoretically, the vanishing of waves below the lowest frequency of the observed  
<sup>348</sup> wave power spectrum (denoted as  $f_{\min}$ ) may be simply a result of a decrease of  
<sup>349</sup> wave growth, which is due to the hot ion distribution and resonant conditions  
<sup>350</sup> rather than the effect of the cutoff frequency. Therefore, the lower limit of the  
<sup>351</sup>  $H^+$  abundance ratio can be estimated by inserting the relation  $f_{\min} \geq f_{\text{cut}}$  into  
<sup>352</sup> Equation (9).

### <sup>353</sup> The Convective Growth Rate for Unguided Mode around <sup>354</sup> $H^+$ Gyrofrequency

<sup>355</sup> For a given ion phase space density distribution  $F(v_{\parallel}, v_{\perp})$ , the growth rate de-  
<sup>356</sup> pends on the integration of the terms containing  $\partial F(v_{\parallel}, v_{\perp})/\partial v_{\perp}$  and  $\partial F(v_{\parallel}, v_{\perp})/\partial v_{\parallel}$   
<sup>357</sup> along the resonant surface  $v_{\parallel} = (\omega - m\Omega_s)/k_{\parallel}$ . Based on Kennel et al. [63], here,  
<sup>358</sup> we derive a simplified form of the convective growth rate for the unguided mod-  
<sup>359</sup> e near  $H^+$  gyrofrequency to better demonstrate how the  $F(v_{\parallel}, v_{\perp})$  distribution  
<sup>360</sup> leads to wave growth. In the environment of the radiation belt, the Stix pa-  
<sup>361</sup> rameter  $P$  dominates  $L$ ,  $R$  and refractive index  $R_I$ . One can thus simplify the  
<sup>362</sup> imaginary part of the first order of the dispersion function:

$$\begin{aligned} \text{Im } D^{(1)}(\omega, \mathbf{k}) &= -2\pi \sum_s \frac{\omega_{\text{ps}}^2}{\omega |k_{\parallel}|} \int_0^\infty v_{\perp} dv_{\perp} \int_{-\infty}^{+\infty} dv_{\parallel} \sum_m \delta(v_{\parallel} - \frac{\omega - m\Omega_s}{k_{\parallel}}) \\ &\cdot 2Pv_{\perp} [R + L - 2R_I^2] G_{1s}^*, \end{aligned} \quad (10)$$

<sup>365</sup> where

$$\begin{aligned} G_{1s}^* &\approx G_{1s} \frac{1}{2[R + L - 2R_I^2]} [2(L - R_I^2)J_{m+1}^2 + 2(R - n^2)J_{m-1}^2 + R_I^2 \sin^2 \psi (J_{m+1} - J_{m-1})^2] \\ &= \left( \frac{\partial \bar{F}_s}{\partial v_{\perp}} - \frac{k_{\parallel}}{\omega} \frac{\partial \bar{F}_s}{\partial \alpha} \right) \cdot \left[ \frac{L - R_I^2}{R + L - 2R_I^2} J_{m+1} + \frac{R - R_I^2}{R + L - 2R_I^2} J_{m-1} \right]^2. \end{aligned} \quad (11)$$

<sup>368</sup> Following [64], express the magnitude of convective growth rate  $\mathbf{k}_i$  as

$$k_i = - \frac{\text{Im } D^{(1)}(\omega, \mathbf{k})}{\hat{\mathbf{k}} \cdot \partial D^{(0)}/\partial \mathbf{k}}, \quad (12)$$

<sup>370</sup> here

$$\frac{\partial D^{(0)}}{\partial k} = \frac{8P}{k} [\cos^2 \psi R_I^4 - RL]. \quad (13)$$

<sup>372</sup> Considering that the group velocity points in nearly the same direction as the  
<sup>373</sup> wave vector for the unguided mode, one can finally express the component of  
<sup>374</sup>  $\mathbf{k}_i$  in the group velocity direction as:

$$\begin{aligned} \text{375} \quad K_i &= -\hat{\mathbf{k}} \cdot \hat{\mathbf{v}}_g k_i \\ \text{376} \quad &\approx -k_i \\ \text{377} \quad &\approx \frac{1}{2} \pi^2 \sum_s \frac{k \omega_{ps}^2}{|k_\parallel| \omega} \frac{R + L - 2R_I^2}{RL - \cos^2 \psi R_I^4} \int_0^\infty v_\perp^2 G_{1s}^* dv_\perp. \end{aligned} \quad (14)$$

<sup>378</sup> It can be proven that the product of the factors outside the integral is greater  
<sup>379</sup> than zero, therefore, the values of  $G_{1s}^*$  represent the contribution to wave growth  
<sup>380</sup> by hot ions with a given energy range.

<sup>381</sup> The derivatives of the phase space density ( $F = j/p^2$ ) with respect to the  
<sup>382</sup> energy  $E$  and pitch angle  $\alpha$  for each ion species can be obtained based on obser-  
<sup>383</sup> vation. As the major ions H<sup>+</sup> dominate the wave growth, here the phase space  
<sup>384</sup> density  $F$  is estimated approximately from the H<sup>+</sup> flux collected by HOPE and  
<sup>385</sup> RBSPICE. HOPE measures the H<sup>+</sup> flux ( $j_{H+}$ ) with the energy from several eV  
<sup>386</sup> to  $\sim 50$  keV, while the RBSPICE measures  $j_{H+}$  from  $\sim 50$  keV to  $\sim 600$  keV.  
<sup>387</sup> These two energy ranges cover the main structures of the ring current H<sup>+</sup> and  
<sup>388</sup> are sufficient to evaluate the linear instability. The HOPE flux is multiplied by  
<sup>389</sup> a factor of 3 so that the mismatch between the low-energy part of RBSPICE  
<sup>390</sup> and the high-energy part of HOPE can be eliminated [65, 66]. The distribution  
<sup>391</sup> of  $F(E, \alpha)$  is fitted along pitch angle  $\alpha$  for each fixed energy channel, and the  
<sup>392</sup> required derivatives are then approximated with the help of B-spline interpola-  
<sup>393</sup> tion. The details regarding this technique follow [67].  $D^{(0)}$  and  $D^{(1)}$  also depend  
<sup>394</sup> on the background magnetic field, the plasma number density  $n_e$  and the ion  
<sup>395</sup> abundance ratios  $\eta_s = n_s/n_e$  (where s denotes the particle species). The mag-  
<sup>396</sup> netic field is measured by MAG, the local plasma density is measured HFR, and  
<sup>397</sup> the ion abundance ratios are determined via the plasma diagnostics.

## <sup>398</sup> Data Availability

<sup>399</sup> The particle data are available from <http://www.RBSP-ect.lanl.gov/> and  
<sup>400</sup> <http://rbspice.ftecs.com/Data.html>. The electric field data are available  
<sup>401</sup> from <http://www.space.umn.edu/rbspefw-data/>. The magnetic field data  
<sup>402</sup> are available from <http://emfisis.physics.uiowa.edu/Flight/>. The mag-  
<sup>403</sup> netic field model can be obtained from [http://geo.phys.spbu.ru/%7etsyganenko/](http://geo.phys.spbu.ru/%7etsyganenko/modeling.html)  
<sup>404</sup> [modeling.html](http://geo.phys.spbu.ru/%7etsyganenko/modeling.html). The geomagnetic indices are available from [https://omniweb.](https://omniweb.gsfc.nasa.gov/)  
<sup>405</sup> [gsfc.nasa.gov/](https://omniweb.gsfc.nasa.gov/)

## <sup>406</sup> References

- <sup>407</sup> [1] Yoshiya Kasahara et al. “Ion cyclotron emissions observed by the satellite  
<sup>408</sup> Akebono in the vicinity of the magnetic equator”. In: *Radio Sci.* 27.2 (Apr.  
<sup>409</sup> 1992), pp. 347–362. DOI: 10.1029/91RS01872.

- 410 [2] K. Keika et al. “Global characteristics of electromagnetic ion cyclotron  
411 waves: Occurrence rate and its storm dependence”. In: *J. Geophys. Res.*  
412 (*Space Physics*) 118 (July 2013), pp. 4135–4150. DOI: 10.1002/jgra.1  
413 50385.
- 414 [3] N. P. Meredith et al. “Global morphology and spectral properties of EMIC  
415 waves derived from CRRES observations”. In: *J. Geophys. Res. (Space*  
416 *Physics*) 119 (July 2014), pp. 5328–5342. DOI: 10.1002/2014JA020064.
- 417 [4] Xiongdong Yu et al. “In situ observations of EMIC waves in O<sup>+</sup> band  
418 by the Van Allen Probe A”. In: *Geophys. Res. Lett.* 42.5 (Mar. 2015),  
419 pp. 1312–1317. DOI: 10.1002/2015GL063250.
- 420 [5] A. A. Saikin et al. “The occurrence and wave properties of H<sup>+</sup>-, He<sup>+</sup>-  
421 , and O<sup>+</sup>-band EMIC waves observed by the Van Allen Probes”. In: *J.*  
422 *Geophys. Res. (Space Physics)* 120 (Sept. 2015), pp. 7477–7492. DOI: 10.  
423 1002/2015JA021358.
- 424 [6] D. Wang et al. “Statistical characteristics of EMIC waves: Van Allen Probe  
425 observations”. In: *J. Geophys. Res. (Space Physics)* 120 (June 2015), p-  
426 p. 4400–4408. DOI: 10.1002/2015JA021089.
- 427 [7] X. Y. Wang et al. “The occurrence and wave properties of EMIC waves  
428 observed by the Magnetospheric Multiscale (MMS) mission”. In: *J. Geo-*  
429 *phys. Res. (Space Physics)* 122.8 (Aug. 2017), pp. 8228–8240. DOI: 10.  
430 1002/2017JA024237.
- 431 [8] Huayue Chen et al. “Analyzing EMIC Waves in the Inner Magnetosphere  
432 Using Long-Term Van Allen Probes Observations”. In: *J. Geophys. Res.*  
433 (*Space Physics*) 124.9 (Sept. 2019), pp. 7402–7412. DOI: 10.1029/2019JA026965.
- 434 [9] S. S. Tetrck et al. “Location of intense electromagnetic ion cyclotron  
435 (EMIC) wave events relative to the plasmapause: Van Allen Probes obser-  
436 vations”. In: *J. Geophys. Res. (Space Physics)* 122 (Apr. 2017), pp. 4064–  
437 4088. DOI: 10.1002/2016JA023392.
- 438 [10] R. M. Thorne et al. “Interaction of EMIC Waves With Thermal Plasma  
439 and Radiation Belt Particles”. In: *Magnetospheric ULF Waves: Synthesis*  
440 and New Directions. Ed. by K. Takahashi et al. Vol. 169. Washington DC  
441 American Geophysical Union Geophysical Monograph Series. 2006, p. 213.  
442 DOI: 10.1029/169GM14.
- 443 [11] Y. Miyoshi et al. “Precipitation of radiation belt electrons by EMIC waves,  
444 observed from ground and space”. In: *Geophys. Res. Lett.* 35, L23101 (Dec.  
445 2008), p. 23101. DOI: 10.1029/2008GL035727.
- 446 [12] Z. Wang et al. “Statistical characteristics of EMIC wave-driven relativistic  
447 electron precipitation with observations of POES satellites: Revisit”. In:  
448 *J. Geophys. Res. (Space Physics)* 119 (July 2014), pp. 5509–5519. DOI:  
449 10.1002/2014JA020082.

- 450 [13] M. E. Usanova et al. “Effect of EMIC waves on relativistic and ultrarelativistic electron populations: Ground-based and Van Allen Probes observations”. In: *Geophys. Res. Lett.* 41 (Mar. 2014), pp. 1375–1381. DOI: 10.1002/2013GL059024.
- 451
- 452
- 453
- 454 [14] L. W. Blum et al. “Observations of coincident EMIC wave activity and duskside energetic electron precipitation on 18-19 January 2013”. In: *Geophys. Res. Lett.* 42.14 (July 2015), pp. 5727–5735. DOI: 10.1002/2015GL065245.
- 455
- 456
- 457 [15] C. J. Rodger et al. “High-resolution in situ observations of electron precipitation-causing EMIC waves”. In: *Geophys. Res. Lett.* 42 (Nov. 2015), pp. 9633–9641. DOI: 10.1002/2015GL066581.
- 458
- 459
- 460 [16] X. J. Zhang et al. “Physical mechanism causing rapid changes in ultrarelativistic electron pitch angle distributions right after a shock arrival: Evaluation of an electron dropout event”. In: *J. Geophys. Res. (Space Physics)* 121.9 (Sept. 2016), pp. 8300–8316. DOI: 10.1002/2016JA022517.
- 461
- 462
- 463
- 464 [17] Z. Su et al. “Rapid Loss of Radiation Belt Relativistic Electrons by EMIC Waves”. In: *J. Geophys. Res. (Space Physics)* 122 (Oct. 2017), pp. 9880–9897. DOI: 10.1002/2017JA024169.
- 465
- 466
- 467 [18] L. Bingley et al. “The Evolution of a Pitch-Angle “Bite-Out” Scattering Signature Caused by EMIC Wave Activity: A Case Study”. In: *J. Geophys. Res. (Space Physics)* 124.7 (July 2019), pp. 5042–5055. DOI: 10.1029/2018JA026292.
- 468
- 469
- 470
- 471 [19] L. W. Blum et al. “Persistent EMIC Wave Activity Across the Nightside Inner Magnetosphere”. In: *Geophys. Res. Lett.* 47.6, e87009 (Mar. 2020), e87009. DOI: 10.1029/2020GL087009.
- 472
- 473
- 474 [20] Hui Zhu et al. “Direct Evidence of the Pitch Angle Scattering of Relativistic Electrons Induced by EMIC Waves”. In: *Geophys. Res. Lett.* 47.4, e85637 (Feb. 2020), e85637. DOI: 10.1029/2019GL085637.
- 475
- 476
- 477 [21] J. L. Rauch and A. Roux. “Ray tracing of ULF waves in a multicomponent magnetospheric plasma - Consequences for the generation mechanism of ion cyclotron waves”. In: *J. Geophys. Res.* 87 (Oct. 1982), pp. 8191–8198. DOI: 10.1029/JA087iA10p08191.
- 478
- 479
- 480
- 481 [22] R. B. Horne and R. M. Thorne. “On the preferred source location for the convective amplification of ion cyclotron waves”. In: *J. Geophys. Res.* 98 (June 1993), pp. 9233–9247. DOI: 10.1029/92JA02972.
- 482
- 483
- 484 [23] John M. Cornwall. “Cyclotron Instabilities and Electromagnetic Emission in the Ultra Low Frequency and Very Low Frequency Ranges”. In: *J. Geophys. Res. (Space Physics)* 70.1 (Jan. 1965), pp. 61–69. DOI: 10.1029/JZ070i001p00061.
- 485
- 486
- 487
- 488 [24] C. F. Kennel and H. E. Petschek. “Limit on Stably Trapped Particle Fluxes”. In: *J. Geophys. Res.* 71 (Jan. 1966), p. 1.
- 489
- 490 [25] B. J. Anderson and D. C. Hamilton. “Electromagnetic ion cyclotron waves stimulated by modest magnetospheric compressions”. In: *J. Geophys. Res. (Space Physics)* 98 (July 1993), p. 11. DOI: 10.1029/93JA00605.
- 491
- 492

- 493 [26] L. Chen et al. “Global simulation of EMIC wave excitation during the 21  
 494 April 2001 storm from coupled RCM-RAM-HOTRAY modeling”. In: *J.  
 495 Geophys. Res.* 115, A07209 (July 2010), p. 7209. DOI: 10.1029/2009JA015075.
- 496 [27] Manish Mithaiwala et al. “Convective amplification of electromagnetic  
 497 ion cyclotron waves from ring-distribution protons in the inner magne-  
 498 tosphere”. In: *J. Geophys. Res. (Space Physics)* 118.12 (Dec. 2013), p-  
 499 p. 7538–7544. DOI: 10.1002/2013JA019134. arXiv:1306.2215 [physics.space-ph].
- 500 [28] X. Yu et al. “Excitation of oblique O<sup>+</sup> band EMIC waves in the inner  
 501 magnetosphere driven by hot H<sup>+</sup> with ring velocity distributions”. In: *J.  
 502 Geophys. Res. (Space Physics)* 121 (Nov. 2016), p. 11. DOI: 10.1002/  
 503 2016JA023221.
- 504 [29] M. F. Thomsen et al. “Ring/Shell Ion Distributions at Geosynchronous  
 505 Orbit”. In: *J. Geophys. Res. (Space Physics)* 122.12 (Dec. 2017), pp. 12,055–  
 506 12,071. DOI: 10.1002/2017JA024612.
- 507 [30] B. Remya et al. “Ion Injection Triggered EMIC Waves in the Earth’s  
 508 Magnetosphere”. In: *J. Geophys. Res. (Space Physics)* 123 (June 2018),  
 509 pp. 4921–4938. DOI: 10.1029/2018JA025354.
- 510 [31] J. U. Kozyra et al. “Effects of energetic heavy ions on electromagnetic ion  
 511 cyclotron wave generation in the plasmapause region”. In: *J. Geophys.  
 512 Res. (Space Physics)* 89.A4 (Apr. 1984), pp. 2217–2234. DOI: 10.1029/  
 513 JA089iA04p02217.
- 514 [32] S. Peter Gary. *Theory of Space Plasma Microinstabilities*. 1993.
- 515 [33] M. J. Engebretson et al. “Van Allen probes, NOAA, GOES, and ground  
 516 observations of an intense EMIC wave event extending over 12 h in mag-  
 517 netic local time”. In: *J. Geophys. Res. (Space Physics)* 120 (July 2015),  
 518 pp. 5465–5488. DOI: 10.1002/2015JA021227.
- 519 [34] L. W. Blum et al. “EMIC wave scale size in the inner magnetosphere:  
 520 Observations from the dual Van Allen Probes”. In: *Geophys. Res. Lett.* 44  
 521 (Feb. 2017), pp. 1227–1233. DOI: 10.1002/2016GL072316.
- 522 [35] Si Liu et al. “Magnetospheric Multiscale Observation of Quasiperiod-  
 523 ic EMIC Waves Associated With Enhanced Solar Wind Pressure”. In:  
 524 *Geophys. Res. Lett.* 46.13 (July 2019), pp. 7096–7104. DOI: 10.1029/  
 525 2019GL083421.
- 526 [36] L. Chen, R. M. Thorne, and R. B. Horne. “Simulation of EMIC wave  
 527 excitation in a model magnetosphere including structured high-density  
 528 plumes”. In: *J. Geophys. Res. (Space Physics)* 114, A07221 (July 2009),  
 529 A07221. DOI: 10.1029/2009JA014204.
- 530 [37] M. de Soria-Santacruz, M. Spasojevic, and L. Chen. “EMIC waves growth  
 531 and guiding in the presence of cold plasma density irregularities”. In:  
 532 *Geophys. Res. Lett.* 40 (May 2013), pp. 1940–1944. DOI: 10.1002/grl.  
 533 50484.

- 534 [38] J.-C. Zhang et al. “Excitation of EMIC waves detected by the Van Allen  
 535 Probes on 28 April 2013”. In: *Geophys. Res. Lett.* 41 (June 2014), p-  
 536 p. 4101–4108. DOI: 10.1002/2014GL060621.
- 537 [39] R. C. Allen et al. “A statistical study of EMIC waves observed by Cluster:  
 538 2. Associated plasma conditions”. In: *J. Geophys. Res. (Space Physics)*  
 539 121.7 (July 2016), pp. 6458–6479. DOI: 10.1002/2016JA022541.
- 540 [40] Zhigang Yuan et al. “Simultaneous trapping of EMIC and MS waves by  
 541 background plasmas”. In: *J. Geophys. Res. (Space Physics)* 0.ja (2019).  
 542 DOI: 10.1029/2018JA026149.
- 543 [41] H. Zhao et al. “The evolution of ring current ion energy density and energy  
 544 content during geomagnetic storms based on Van Allen Probes measure-  
 545 ments”. In: *J. Geophys. Res. (Space Physics)* 120.9 (Sept. 2015), pp. 7493–  
 546 7511. DOI: 10.1002/2015JA021533.
- 547 [42] R. B. Horne and R. M. Thorne. “Convective instabilities of electromag-  
 548 netic ion cyclotron waves in the outer magnetosphere”. In: *J. Geophys.  
 549 Res.* 99 (Sept. 1994), p. 17259. DOI: 10.1029/94JA01259.
- 550 [43] B. H. Mauk et al. “Science Objectives and Rationale for the Radiation  
 551 Belt Storm Probes Mission”. In: *Space. Sci. Rev.* 179 (Nov. 2013), pp. 3–  
 552 27. DOI: 10.1007/s11214-012-9908-y.
- 553 [44] D. G. Mitchell et al. “Radiation Belt Storm Probes Ion Composition Ex-  
 554 periment (RBSPICE)”. In: *Space Sci. Rev.* 179.1-4 (Nov. 2013), pp. 263–  
 555 308. DOI: 10.1007/s11214-013-9965-x.
- 556 [45] H. O. Funsten et al. “Helium, Oxygen, Proton, and Electron (HOPE)  
 557 Mass Spectrometer for the Radiation Belt Storm Probes Mission”. In:  
 558 *Space. Sci. Rev.* 179 (Nov. 2013), pp. 423–484. DOI: 10.1007/s11214-  
 559 013-9968-7.
- 560 [46] W. S. Kurth et al. “Electron densities inferred from plasma wave spectra  
 561 obtained by the Waves instrument on Van Allen Probes”. In: *J. Geo-  
 562 phys. Res. (Space Physics)* 120 (Feb. 2015), pp. 904–914. DOI: 10.1002/  
 563 2014JA020857.
- 564 [47] C. A. Kletzing et al. “The Electric and Magnetic Field Instrument Suite  
 565 and Integrated Science (EMFISIS) on RBSP”. In: *Space. Sci. Rev.* 179  
 566 (Nov. 2013), pp. 127–181. DOI: 10.1007/s11214-013-9993-6.
- 567 [48] B. Ni et al. “Resonant scattering of outer zone relativistic electrons by  
 568 multiband EMIC waves and resultant electron loss time scales”. In: *J.  
 569 Geophys. Res. (Space Physics)* 120 (Sept. 2015), pp. 7357–7373. DOI: 10.  
 570 1002/2015JA021466.
- 571 [49] B. Wang et al. “Nonlinear Landau resonant scattering of near-equatorially  
 572 mirroring radiation belt electrons by oblique EMIC waves”. In: *Geophys.  
 573 Res. Lett.* 43 (2016), pp. 3628–3636. DOI: 10.1002/2016GL068467.

- 574 [50] G. Wang et al. “Nonlinear fundamental and harmonic cyclotron resonant  
 575 scattering of radiation belt ultrarelativistic electrons by oblique monochro-  
 576 matic EMIC waves”. In: *J. Geophys. Res. (Space Physics)* 122 (Feb. 2017),  
 577 pp. 1928–1945. DOI: 10.1002/2016JA023451.
- 578 [51] Dae-Young Lee, Dae-Kyu Shin, and Cheong-Rim Choi. “Effects of Oblique  
 579 Wave Normal Angle and Noncircular Polarization of Electromagnetic Ion  
 580 Cyclotron Waves on the Pitch Angle Scattering of Relativistic Electrons”.  
 581 In: *J. Geophys. Res. (Space Physics)* 123.6 (June 2018), pp. 4556–4573.  
 582 DOI: 10.1029/2018JA025342.
- 583 [52] Song Fu et al. “Interactions between H<sup>+</sup> band EMIC waves and radia-  
 584 tion belt relativistic electrons: Comparisons of test particle simulations  
 585 with quasi-linear calculations”. In: *Phys. Plasmas* 26.3, 032901 (2019),  
 586 p. 032901. DOI: 10.1063/1.5054809.
- 587 [53] Xing Cao et al. “Bounce resonance scattering of radiation belt electrons  
 588 by H<sup>+</sup> band EMIC waves”. In: *J. Geophys. Res. (Space Physics)* 122.2  
 589 (2017), pp. 1702–1713. DOI: 10.1002/2016JA023607.
- 590 [54] X. Cao et al. “Sensitivity of EMIC Wave-Driven Scattering Loss of Ring  
 591 Current Protons to Wave Normal Angle Distribution”. In: *Geophys. Res.  
 592 Lett.* 46 (Jan. 2019), pp. 590–598. DOI: 10.1029/2018GL081550.
- 593 [55] Z. Yuan et al. “Cold electron heating by EMIC waves in the plasmaspheric  
 594 plume with observations of the Cluster satellite”. In: *Geophys. Res. Lett.*  
 595 41 (Mar. 2014), pp. 1830–1837. DOI: 10.1002/2014GL059241.
- 596 [56] Ch. Katsavrias et al. “Highly Relativistic Electron Flux Enhancement  
 597 During the Weak Geomagnetic Storm of April-May 2017”. In: *J. Geophys.  
 598 Res. (Space Physics)* 124.6 (June 2019), pp. 4402–4413. DOI: 10.1029/  
 599 2019JA026743. arXiv:1902.00960 [physics.space-ph].
- 600 [57] O. Santolík, M. Parrot, and F. Lefèuvre. “Singular value decomposition  
 601 methods for wave propagation analysis”. In: *Radio Sci.* 38, 1010 (Feb.  
 602 2003), p. 1010. DOI: 10.1029/2000RS002523.
- 603 [58] O. Santolík et al. “Survey of Poynting flux of whistler mode chorus in  
 604 the outer zone”. In: *J. Geophys. Res. (Space Physics)* 115, A00F13 (July  
 605 2010), A00F13. DOI: 10.1029/2009JA014925.
- 606 [59] T. H. Stix. *Waves in Plasmas*. New York: American Institute of Physics,  
 607 1992.
- 608 [60] R. L. Smith and Neil Brice. “Propagation in Multicomponent Plasmas”.  
 609 In: *J. Geophys. Res.* 69.23 (Dec. 1964), pp. 5029–5040. DOI: 10.1029/  
 610 JZ069i023p05029.
- 611 [61] X. Tao and J. Bortnik. “Nonlinear interactions between relativistic radia-  
 612 tion belt electrons and oblique whistler mode waves”. In: *Nonlinear Proc.  
 613 Geoph.* 17 (Oct. 2010), pp. 599–604. DOI: 10.5194/npg-17-599-2010.

- 614 [62] J. Bortnik and R. M. Thorne. “Transit time scattering of energetic elec-  
615 trons due to equatorially confined magnetosonic waves”. In: *J. Geophys.*  
616 *Res. (Space Physics)* 115, A07213 (July 2010), A07213. DOI: 10.1029/  
617 2010JA015283.
- 618 [63] C. Kennel. “Low-Frequency Whistler Mode”. In: *Phys. Fluids* 9 (Nov.  
619 1966), pp. 2190–2202. DOI: 10.1063/1.1761588.
- 620 [64] L. Chen et al. “Global simulation of magnetosonic wave instability in the  
621 storm time magnetosphere”. In: *J. Geophys. Res. (Space Physics)* 115,  
622 A11222 (Nov. 2010), A11222. DOI: 10.1029/2010JA015707.
- 623 [65] Kyungguk Min et al. “Second harmonic poloidal waves observed by Van  
624 Allen Probes in the dusk-midnight sector”. In: *J. Geophys. Res. (Space*  
625 *Physics)* 122.3 (Mar. 2017), pp. 3013–3039. DOI: 10.1002/2016JA023770.
- 626 [66] L. M. Kistler et al. “The source of O<sup>+</sup> in the storm time ring current”. In:  
627 *J. Geophys. Res. (Space Physics)* 121.6 (June 2016), pp. 5333–5349. DOI:  
628 10.1002/2015JA022204.
- 629 [67] N. Liu et al. “Prompt Disappearance and Emergence of Radiation Belt  
630 Magnetosonic Waves Induced by Solar Wind Dynamic Pressure Variations”. In:  
631 *Geophys. Res. Lett.* 45 (Jan. 2018), pp. 585–594. DOI: 10.1002/  
632 2017GL076382.

# Figures

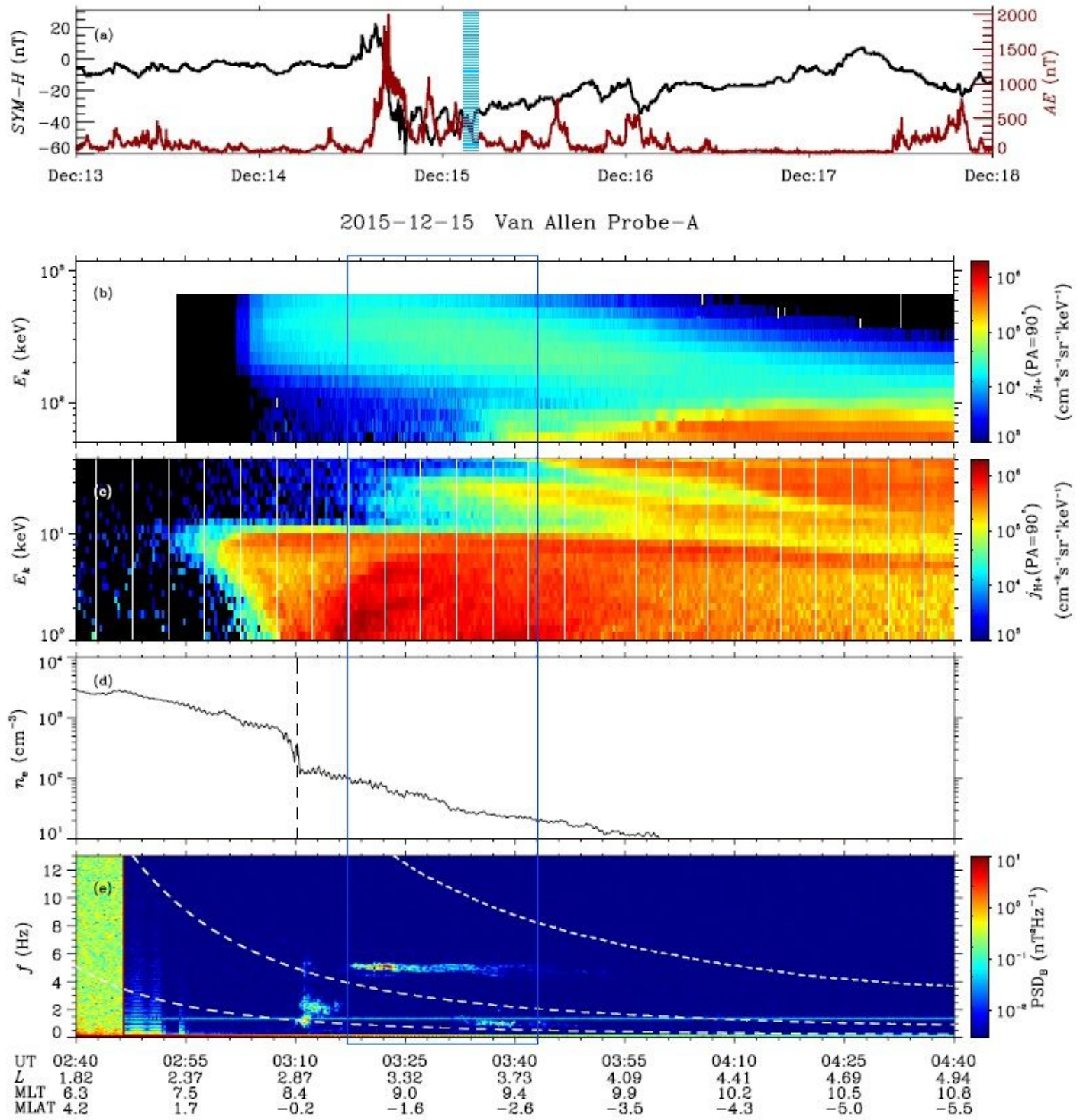


**Figure 1**

Overview of the background conditions of the wave event recorded by Van Allen Probe A on 15 December 2015 (see Manuscript file for full caption.)

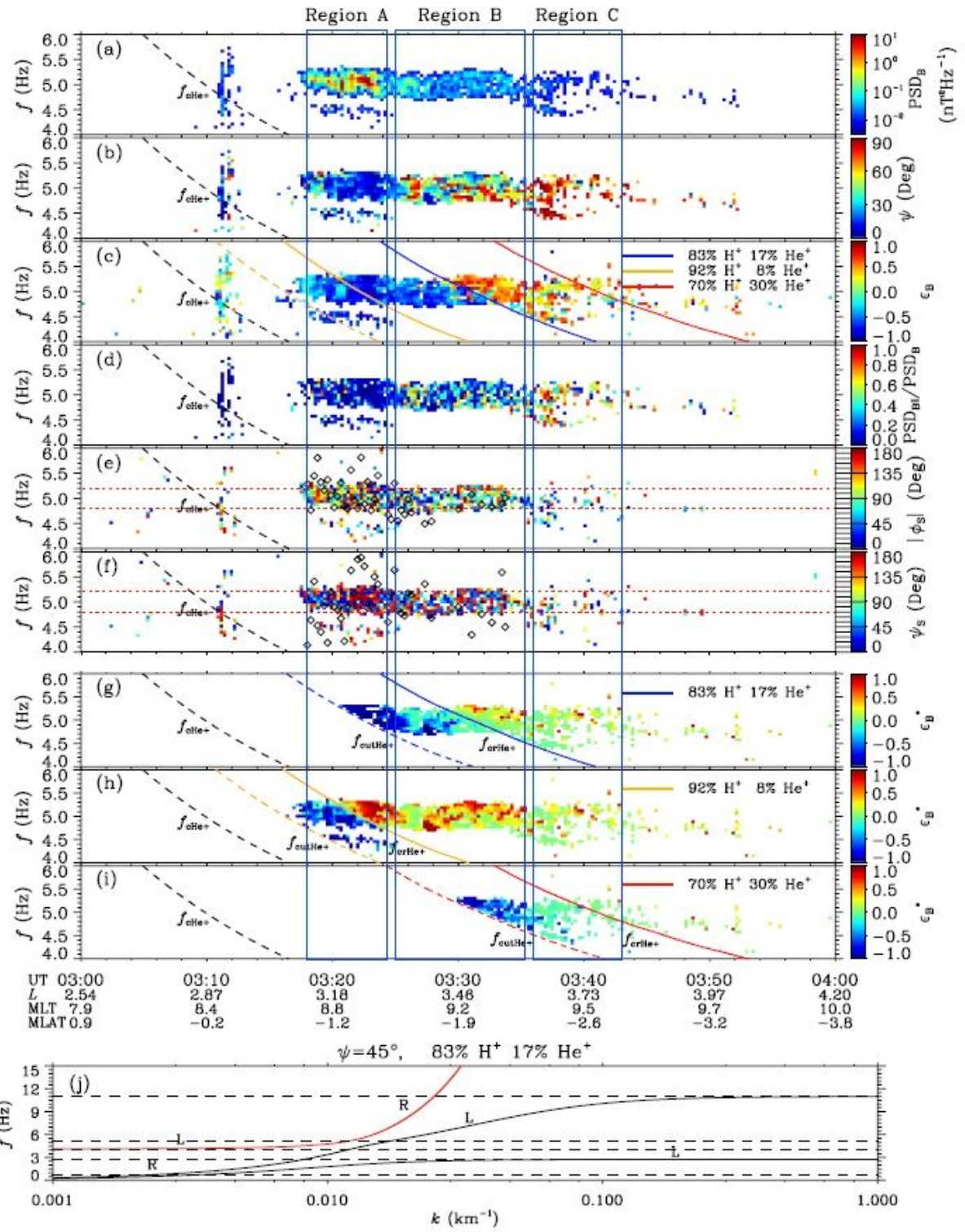


**Figure 2**

Analyses of wave properties and wave mode. (see Manuscript file for full caption.)

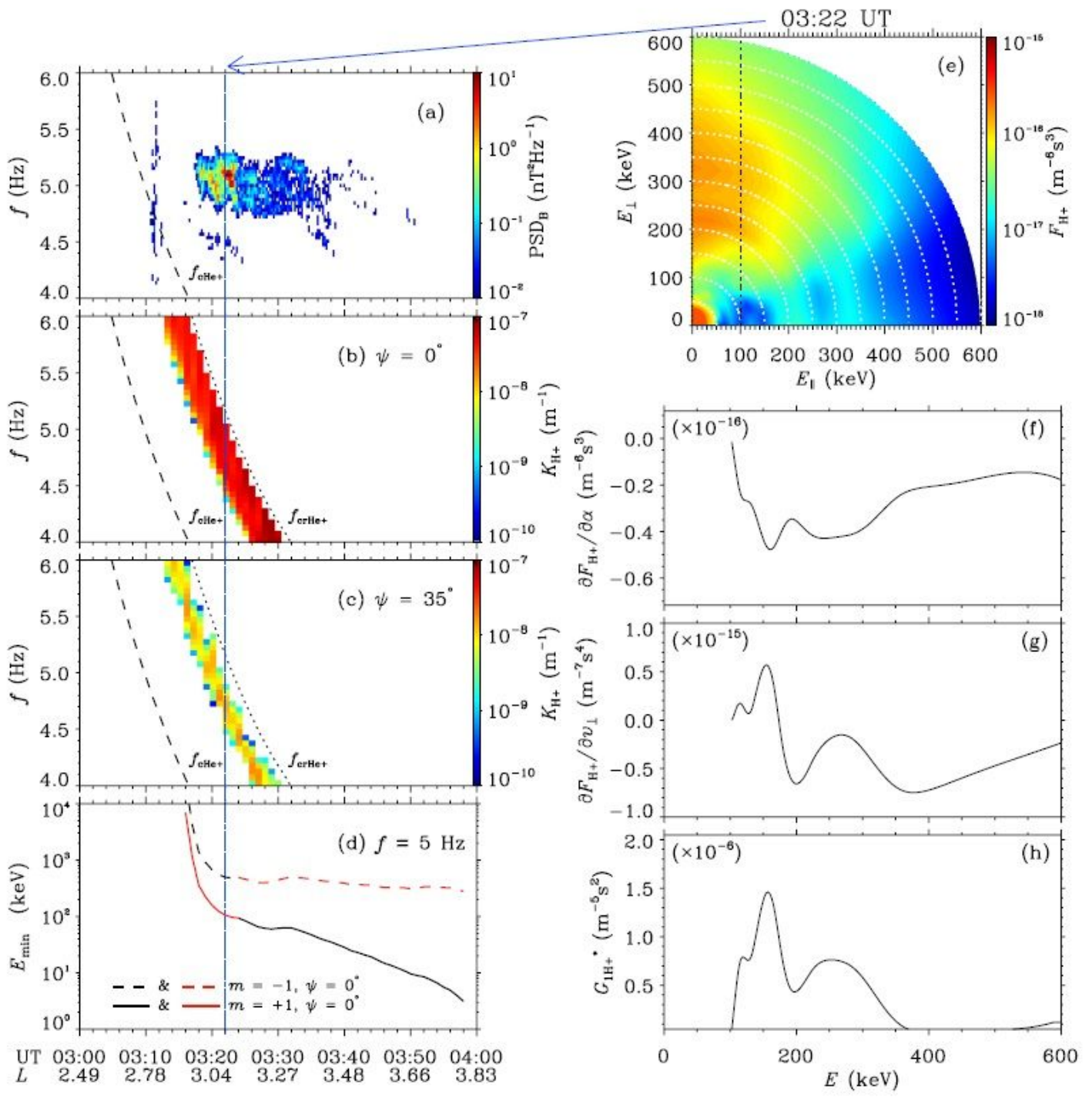


**Figure 3**

Wave growth analyses. (see Manuscript file for full caption.)

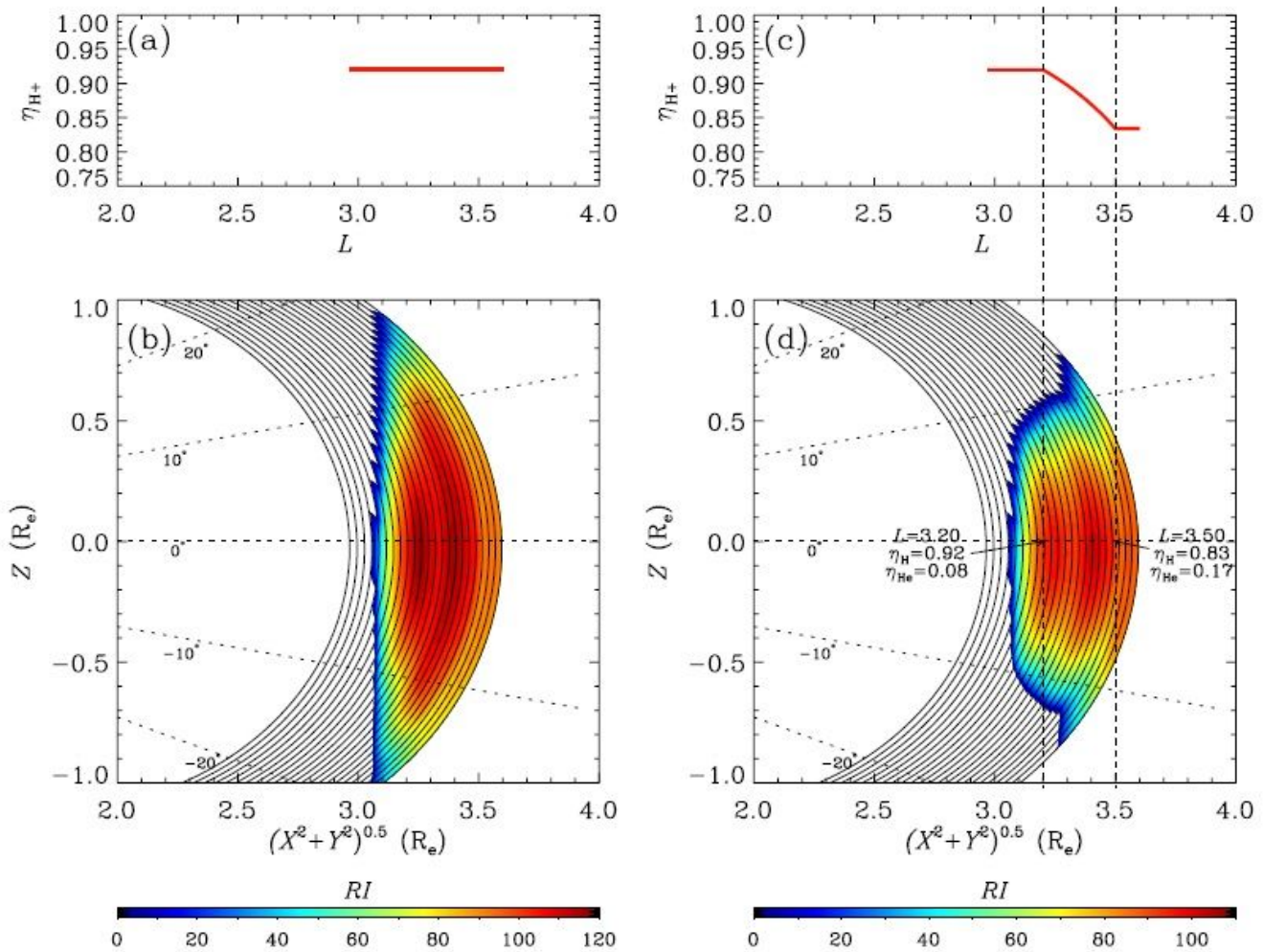


**Figure 4**

The distribution of the refractive index RI in a plasma environment with the ion abundance ratio  $n_{\text{H}^+}$  (see Manuscript file for full caption.)

## Supplementary Files

This is a list of supplementary files associated with this preprint. Click to download.

- [supplementarydocument.pdf](#)